Title

Safety assessment in macaques of light exposures for functional two-photon ophthalmoscopy in humans.

Journal

Biomedical Optics Express, 7(12)

ISSN

2156-7085

Authors

Schwarz, Christina
Sharma, Robin
Fischer, William
et al.

Publication Date

2016-12-01

DOI

10.1364/BOE.7.005148

Peer reviewed

Research Article | Vol. 7, No. 12 | 1 Dec 2016 | BIOMEDICAL OPTICS EXPRESS 5148

Biomedical Optics EXPRESS

Safety assessment in macaques of light exposures for functional two-photon ophthalmoscopy in humans

CHRISTINA SCHWARZ,[1,*] ROBIN SHARMA,[1] WILLIAM S. FISCHER,[2] MINA CHUNG,[1,2] GRAZYNA PALCZEWSKA,[3] KRZYSZTOF PALCZEWSKI,[4] DAVID R. WILLIAMS,[1,2,5] AND JENNIFER J. HUNTER[1,2,6]

[1]*Center for Visual Science, University of Rochester, Rochester, NY, USA*
[2]*Flaum Eye Institute, University of Rochester, Rochester, NY, USA*
[3]*Department of Medical Devices, Polgenix Inc., Cleveland, OH, USA*
[4]*Department of Pharmacology, Cleveland Center for Membrane and Structural Biology, School of Medicine, Case Western Reserve University, Cleveland, OH, USA*
[5]*The Institute of Optics, University of Rochester, Rochester, NY, USA*
[6]*Department of Biomedical Engineering, University of Rochester, Rochester, NY, USA*
[*]*cschwarz@ur.rochester.edu*

Abstract: Two-photon ophthalmoscopy has potential for *in vivo* assessment of function of normal and diseased retina. However, light safety of the sub-100 fs laser typically used is a major concern and safety standards are not well established. To test the feasibility of safe *in vivo* two-photon excitation fluorescence (TPEF) imaging of photoreceptors in humans, we examined the effects of ultrashort pulsed light and the required light levels with a variety of clinical and high resolution imaging methods in macaques. The only measure that revealed a significant effect due to exposure to pulsed light within existing safety standards was infrared autofluorescence (IRAF) intensity. No other structural or functional alterations were detected by other imaging techniques for any of the exposures. Photoreceptors and retinal pigment epithelium appeared normal in adaptive optics images. No effect of repeated exposures on TPEF time course was detected, suggesting that visual cycle function was maintained. If IRAF reduction is hazardous, it is the only hurdle to applying two-photon retinal imaging in humans. To date, no harmful effects of IRAF reduction have been detected.

OCIS codes: (110.1080) Active or adaptive optics; (190.0190) Nonlinear optics; (330.3350) Vision - laser damage.

References and links

1. A. C. Bird, "Retinal photoreceptor dystrophies LI. Edward Jackson Memorial Lecture," Am. J. Ophthalmol. **119**(5), 543–562 (1995).
2. E. L. Berson, "Retinitis pigmentosa: The Friedenwald lecture," Invest. Ophthalmol. Vis. Sci. **34**(5), 1659–1676 (1993).
3. C. P. Hamel, "Cone rod dystrophies," Orphanet J. Rare Dis. **2**(1), 7 (2007).
4. R. N. Weinreb, T. Aung, and F. A. Medeiros, "The Pathophysiology and Treatment of Glaucoma: a Review," JAMA **311**(18), 1901–1911 (2014).
5. E. E. Sutter, "Noninvasive Testing Methods: Multifocal Electrophysiology," Encycl. Eye. **3**, 142–160 (2010).
6. V. C. Greenstein, K. Holopigian, W. Seiple, R. E. Carr, and D. C. Hood, "Atypical multifocal ERG responses in patients with diseases affecting the photoreceptors," Vision Res. **44**(25), 2867–2874 (2004).
7. W. A. H. Rushton, "The difference spectrum and the photosensitivity of rhodopsin in the living human eye," J. Physiol. **134**(1), 11–29 (1956).
8. K. Grieve and A. Roorda, "Intrinsic signals from human cone photoreceptors," Invest. Ophthalmol. Vis. Sci. **49**(2), 713–719 (2008).
9. K. Tsunoda, G. Hanazono, K. Inomata, Y. Kazato, W. Suzuki, and M. Tanifuji, "Origins of retinal intrinsic signals: a series of experiments on retinas of macaque monkeys," Jpn. J. Ophthalmol. **53**(4), 297–314 (2009).
10. B. D. Masella, J. J. Hunter, and D. R. Williams, "New wrinkles in retinal densitometry," Invest. Ophthalmol. Vis. Sci. **55**(11), 7525–7534 (2014).
11. W. Denk, J. H. Strickler, and W. W. Webb, "Two-photon laser scanning fluorescence microscopy," Science **248**(4951), 73–76 (1990).
12. K. Svoboda and R. Yasuda, "Principles of two-photon excitation microscopy and its applications to

#276053 http://dx.doi.org/10.1364/BOE.7.005148
Journal © 2016 Received 20 Sep 2016; revised 8 Nov 2016; accepted 9 Nov 2016; published 16 Nov 2016

Biomedical Optics EXPRESS

neuroscience," Neuron **50**(6), 823–839 (2006).
13. F. Helmchen, "Two-Photon Functional Imaging of Neuronal Activity," in *In Vivo Optical Imaging of Brain Function*, R. D. Frostig, ed. (CRC Press, 2009), p. 428.
14. M. Göppert, "Über die Wahrscheinlichkeit des Zusammenwirkens zweier Lichtquanten in einem Elementarakt," Naturwissenschaften **17**, 932 (1929).
15. M. Göppert-Mayer, "Ueber Elementrarakte mit zwei Quantenspruengen," Ann. Phys. **114**, 273 (1931).
16. A. Diaspro, G. Chirico, and M. Collini, "Two-photon fluorescence excitation and related techniques in biological microscopy," Q. Rev. Biophys. **38**(2), 97–166 (2005).
17. S. Huang, A. A. Heikal, and W. W. Webb, "Two-Photon Fluorescence Spectroscopy and Microscopy of NAD(P)H and Flavoprotein," Biophys. J. **82**(5), 2811–2825 (2002).
18. W. R. Zipfel, R. M. Williams, R. Christie, A. Y. Nikitin, B. T. Hyman, and W. W. Webb, "Live tissue intrinsic emission microscopy using multiphoton-excited native fluorescence and second harmonic generation," Proc. Natl. Acad. Sci. U.S.A. **100**(12), 7075–7080 (2003).
19. C. W. Shuttleworth, "Use of NAD(P)H and flavoprotein autofluorescence transients to probe neuron and astrocyte responses to synaptic activation," Neurochem. Int. **56**(3), 379–386 (2010).
20. Y. Imanishi, M. L. Batten, D. W. Piston, W. Baehr, and K. Palczewski, "Noninvasive two-photon imaging reveals retinyl ester storage structures in the eye," J. Cell Biol. **164**(3), 373–383 (2004).
21. G. Palczewska, T. Maeda, Y. Imanishi, W. Sun, Y. Chen, D. R. Williams, D. W. Piston, A. Maeda, and K. Palczewski, "Noninvasive multiphoton fluorescence microscopy resolves retinol and retinal condensation products in mouse eyes," Nat. Med. **16**(12), 1444–1449 (2010).
22. E. A. Boettner and J. R. Wolter, "Transmission of the ocular media," Invest. Ophthalmol. Vis. Sci. **1**, 776–783 (1962).
23. R. D. Glickman, "Ultraviolet phototoxicity to the retina," Eye Contact Lens **37**(4), 196–205 (2011).
24. J. J. Hunter, B. Masella, A. Dubra, R. Sharma, L. Yin, W. H. Merigan, G. Palczewska, K. Palczewski, and D. R. Williams, "Images of photoreceptors in living primate eyes using adaptive optics two-photon ophthalmoscopy," Biomed. Opt. Express **2**(1), 139–148 (2011).
25. R. Sharma, D. R. Williams, G. Palczewska, K. Palczewski, and J. J. Hunter, "Two-Photon Autofluorescence Imaging Reveals Cellular Structures Throughout the Retina of the Living Primate Eye," Invest. Ophthalmol. Vis. Sci. **57**(2), 632–646 (2016).
26. R. Sharma, C. Schwarz, D. R. Williams, G. Palczewska, K. Palczewski, and J. J. Hunter, "In Vivo Two-Photon Fluorescence Kinetics of Primate Rods and Cones," Invest. Ophthalmol. Vis. Sci. **57**(2), 647–657 (2016).
27. J. C. Saari, "Biochemistry of Visual Pigment Regeneration: the Friedenwald Lecture," Invest. Ophthalmol. Vis. Sci. **41**(2), 337–348 (2000).
28. T. D. Lamb and E. N. Pugh, Jr., "Dark adaptation and the retinoid cycle of vision," Prog. Retin. Eye Res. **23**(3), 307–380 (2004).
29. P. D. Kiser, M. Golczak, A. Maeda, and K. Palczewski, "Key enzymes of the retinoid (visual) cycle in vertebrate retina," Biochim. Biophys. Acta – Mol. Cell Biol. Lipids **1821**(1), 137–151 (2012).
30. P. D. Kiser, M. Golczak, and K. Palczewski, "Chemistry of the retinoid (visual) cycle," Chem. Rev. **114**(1), 194–232 (2014).
31. G. H. Travis, M. Golczak, A. R. Moise, and K. Palczewski, "Diseases caused by defects in the visual cycle: retinoids as potential therapeutic agents," Annu. Rev. Pharmacol. Toxicol. **47**(1), 469–512 (2007).
32. D. A. Thompson and A. Gal, "Vitamin A metabolism in the retinal pigment epithelium: genes, mutations, and diseases," Prog. Retin. Eye Res. **22**(5), 683–703 (2003).
33. E. Tsina, C. Chen, Y. Koutalos, P. Ala-Laurila, M. Tsacopoulos, B. Wiggert, R. K. Crouch, and M. C. Cornwall, "Physiological and microfluorometric studies of reduction and clearance of retinal in bleached rod photoreceptors," J. Gen. Physiol. **124**(4), 429–443 (2004).
34. C. Chen, E. Tsina, M. C. Cornwall, R. K. Crouch, S. Vijayaraghavan, and Y. Koutalos, "Reduction of all-trans retinal to all-trans retinol in the outer segments of frog and mouse rod photoreceptors," Biophys. J. **88**(3), 2278–2287 (2005).
35. P. Ala-Laurila, A. V. Kolesnikov, R. K. Crouch, E. Tsina, S. A. Shukolyukov, V. I. Govardovskii, Y. Koutalos, B. Wiggert, M. E. Estevez, and M. C. Cornwall, "Visual cycle: Dependence of retinol production and removal on photoproduct decay and cell morphology," J. Gen. Physiol. **128**(2), 153–169 (2006).
36. P. A. Liebman, "Microspectrophotometry of retinal cells," Ann. N. Y. Acad. Sci. **157**(1 Data Extracti), 250–264 (1969).
37. P. A. Liebman, "Microspectrophotometry of visual receptors," in *Biochemistry and Physiology of Visual Pigments*, H. Langer, ed. (Springer-Verlag, 1973), pp. 299–305.
38. M. W. Kaplan, "Distribution and axial diffusion of retinol in bleached rod outer segments of frogs (Rana pipiens)," Exp. Eye Res. **40**(5), 721–729 (1985).
39. R. Sharma, C. Schwarz, G. Palczewska, K. Palczewski, D. R. Williams, and J. J. Hunter, "Quantification of retinol production and removal in photoreceptors in the living primate eye using two-photon ophthalmoscopy," Invest. Ophthalmol. Vis. Sci. **57**(12), 2213 (2016).
40. M. Boulton, M. Rózanowska, and B. Rózanowski, "Retinal photodamage," J. Photochem. Photobiol. Bol. Biol. **64**, 144–161 (2001).
41. B. A. Rockwell, R. J. Thomas, and A. Vogel, "Ultrashort laser pulse retinal damage mechanisms and their impact on thresholds," Med. Laser Appl. **25**(2), 84–92 (2010).

Biomedical Optics EXPRESS

42. Laser Institute of America, "ANSI Z136.1 - Safe Use of Lasers," (2014).
43. J. I. W. Morgan, J. J. Hunter, B. Masella, R. Wolfe, D. C. Gray, W. H. Merigan, F. C. Delori, and D. R. Williams, "Light-induced retinal changes observed with high-resolution autofluorescence imaging of the retinal pigment epithelium," Invest. Ophthalmol. Vis. Sci. **49**(8), 3715–3729 (2008).
44. G. M. Pocock, J. W. Oliver, C. S. Specht, J. S. Estep, G. D. Noojin, K. Schuster, and B. A. Rockwell, "High-resolution in vivo imaging of regimes of laser damage to the primate retina," J. Ophthalmol. **2014**, 516854 (2014).
45. B. D. Masella, J. J. Hunter, and D. R. Williams, "Rod photopigment kinetics after photodisruption of the retinal pigment epithelium," Invest. Ophthalmol. Vis. Sci. **55**(11), 7535–7544 (2014).
46. J. J. Hunter, J. I. W. Morgan, W. H. Merigan, D. H. Sliney, J. R. Sparrow, and D. R. Williams, "The susceptibility of the retina to photochemical damage from visible light," Prog. Retin. Eye Res. **31**(1), 28–42 (2012).
47. J. I. W. Morgan, J. J. Hunter, W. H. Merigan, and D. R. Williams, "The reduction of retinal autofluorescence caused by light exposure," Invest. Ophthalmol. Vis. Sci. **50**(12), 6015–6022 (2009).
48. J. Zhang, R. Sabarinathan, T. Bubel, D. R. Williams, and J. J. Hunter, "Action spectrum for photochemical retinal pigment epithelium (RPE) disruption in an in vivo monkey model," Proc. SPIE **9706**, 1–6 (2016).
49. F. C. Delori, C. K. Dorey, G. Staurenghi, O. Arend, D. G. Goger, and J. J. Weiter, "In vivo fluorescence of the ocular fundus exhibits retinal pigment epithelium lipofuscin characteristics," Invest. Ophthalmol. Vis. Sci. **36**(3), 718–729 (1995).
50. C. N. Keilhauer and F. C. Delori, "Near-infrared autofluorescence imaging of the fundus: visualization of ocular melanin," Invest. Ophthalmol. Vis. Sci. **47**(8), 3556–3564 (2006).
51. J. I. W. Morgan, A. Dubra, R. Wolfe, W. H. Merigan, and D. R. Williams, "In vivo autofluorescence imaging of the human and macaque retinal pigment epithelial cell mosaic," Invest. Ophthalmol. Vis. Sci. **50**(3), 1350–1359 (2009).
52. J. Liang, D. R. Williams, and D. T. Miller, "Supernormal vision and high-resolution retinal imaging through adaptive optics," J. Opt. Soc. Am. A **14**(11), 2884–2892 (1997).
53. E. A. Rossi, M. Chung, A. Dubra, J. J. Hunter, W. H. Merigan, and D. R. Williams, "Imaging retinal mosaics in the living eye," Eye (Lond.) **25**(3), 301–308 (2011).
54. A. Dubra, Y. Sulai, J. L. Norris, R. F. Cooper, A. M. Dubis, D. R. Williams, and J. Carroll, "Noninvasive imaging of the human rod photoreceptor mosaic using a confocal adaptive optics scanning ophthalmoscope," Biomed. Opt. Express **2**(7), 1864–1876 (2011).
55. D. A. Baylor, B. J. Nunn, and J. L. Schnapf, "Spectral sensitivity of cones of the monkey Macaca fascicularis," J. Physiol. **390**(1), 145–160 (1987).
56. B. D. Masella, D. R. Williams, W. S. Fischer, E. A. Rossi, and J. J. Hunter, "Long-term reduction in infrared autofluorescence caused by infrared light below the maximum permissible exposure," Invest. Ophthalmol. Vis. Sci. **55**(6), 3929–3938 (2014).
57. A. Dubra and Z. Harvey, "Registration of 2D images from fast scanning ophthalmic instruments," Lect. Notes Comput. Sci. **6204**, 60–71 (2010).
58. G. Palczewska, F. Vinberg, P. Stremplewski, M. P. Bircher, D. Salom, K. Komar, J. Zhang, M. Cascella, M. Wojtkowski, V. J. Kefalov, and K. Palczewski, "Human infrared vision is triggered by two-photon chromophore isomerization," Proc. Natl. Acad. Sci. U.S.A. **111**(50), E5445–E5454 (2014).
59. L. N. Thibos, M. Ye, X. Zhang, and A. Bradley, "The chromatic eye: a new reduced-eye model of ocular chromatic aberration in humans," Appl. Opt. **31**(19), 3594–3600 (1992).
60. Y. Coello, B. Xu, T. L. Miller, V. V. Lozovoy, and M. Dantus, "Group-velocity dispersion measurements of water, seawater, and ocular components using multiphoton intrapulse interference phase scan," Appl. Opt. **46**(35), 8394–8401 (2007).
61. C. P. Cain, R. J. Thomas, G. D. Noojin, D. J. Stolarski, P. K. Kennedy, G. D. Buffington, and B. A. Rockwell, "Sub-50-fs laser retinal damage thresholds in primate eyes with group velocity dispersion, self-focusing and low-density plasmas," Graefes Arch. Clin. Exp. Ophthalmol. **243**(2), 101–112 (2005).
62. A. Vogel, G. Huttmann, G. Paltauf, and J. Noack, "Femtosecond-laser-produced low-density plasmas in transparent biological media: A tool for the creation of chemical, thermal and thermomechanical effects below the optical breakdown threshold," SPIE Photonics West **4633**, 23–37 (2002).
63. A. Vogel, J. Noack, G. Huettmann, and G. Paltauf, "Low-density plasmas below the optical breakdown threshold: potential hazard for multiphoton microscopy, and a tool for the manipulation of intracellular events," SPIE Photonics West **4620**, 202–216 (2002).
64. F. C. Delori, R. H. Webb, and D. H. Sliney; American National Standards Institute, "Maximum permissible exposures for ocular safety (ANSI 2000), with emphasis on ophthalmic devices," J. Opt. Soc. Am. A **24**(5), 1250–1265 (2007).
65. G. J. Brakenhoff, M. Müller, and R. I. Ghauharali, "Analysis of efficiency of two-photon versus single-photon absorption of fluorescence generation in biological objects," J. Microsc. **183**(2), 140–144 (1996).
66. O. A. R. Mahroo and T. D. Lamb, "Recovery of the human photopic electroretinogram after bleaching exposures: estimation of pigment regeneration kinetics," J. Physiol. **554**(2), 417–437 (2004).
67. P. Kayatz, G. Thumann, T. T. Luther, J. F. Jordan, K. U. Bartz-Schmidt, P. J. Esser, and U. Schraermeyer, "Oxidation causes melanin fluorescence," Invest. Ophthalmol. Vis. Sci. **42**(1), 241–246 (2001).
68. Q. Yang, J. Zhang, K. Nozato, K. Saito, D. R. Williams, A. Roorda, and E. A. Rossi, "Closed-loop optical

Biomedical Optics EXPRESS

stabilization and digital image registration in adaptive optics scanning light ophthalmoscopy," Biomed. Opt. Express **5**(9), 3174–3191 (2014).
69. A. Roorda and J. L. Duncan, "Adaptive optics ophthalmoscopy," Annu Rev Vis Sci **1**(1), 19–50 (2015).
70. C. Keller, C. Grimm, A. Wenzel, F. Hafezi, and C. Remé, "Protective effect of halothane anesthesia on retinal light damage: inhibition of metabolic rhodopsin regeneration," Invest. Ophthalmol. Vis. Sci. **42**(2), 476–480 (2001).
71. J. H. Marburger, "Self-focusing: Theory," Prog. Quantum Electron. **4**, 35–110 (1975).
72. R. W. Boyd, S. G. Lukishova, and Y. R. Shen, *Self-Focusing: Past and Present: Fundamentals and Prospects* (Springer, 2009).
73. B. A. Rockwell, W. P. Roach, M. E. Rogers, M. W. Mayo, C. A. Toth, C. P. Cain, and G. D. Noojin, "Nonlinear refraction in vitreous humor," Opt. Lett. **18**(21), 1792–1794 (1993).
74. P. K. Kennedy, "A First-Order Model for Computation of Laser-Induced Breakdown Thresholds in Ocular and Aqueous Media: Part I - Theory," IEEE J. Quantum Electron. **31**(12), 2241–2249 (1995).
75. P. K. Kennedy, S. A. Boppart, D. X. Hammer, B. A. Rockwell, G. D. Noojin, and W. P. Roach, "A First-Order Model for Computation of Laser-Induced Breakdown Thresholds in Ocular and Aqueous Media: II - Comparison to Experiment," IEEE J. Quantum Electron. **31**(12), 2250–2257 (1995).
76. L. V. Keldysh, "Ionization in the field of a strong electromagnetic wave," Sov. Phys. JETP **20**, 1307–1314 (1965).

1. Introduction

In many blinding retinal diseases, severe function loss precedes any detectable structural changes in the retina, impeding a timely diagnosis. Depending on the disease, certain cell types are affected first. Photoreceptor dystrophies [1] initially compromise either rod or cone function [2,3], whereas glaucoma manifests in diminished ganglion cell responses [4]. Objective methods currently used to assess outer retinal function include electroretinography [5,6] and rhodopsin densitometry [7]. However, in both techniques, several retinal layers contribute to the signal, generating artifacts and complicating data interpretation [8–10]. To facilitate the diagnosis and prognosis of retinal diseases as well as the assessment of therapeutic interventions, more reliable, noninvasive methods are needed to evaluate retinal function.

Multiphoton microscopy [11] is a well-established technique for intravital imaging of exogenous functional reporters at subcellular resolution [12,13]. This technique can also be used to image endogenous fluorophores and thus to noninvasively observe biochemical processes as they occur in cells of healthy and diseased tissue. Multiphoton excitation [14–16] offers a special advantage for ophthalmoscopy, because important fluorophores such as NAD(P)H [17–19] and retinoids [20,21] can only be accessed with UV light, a spectral range that is blocked by the anterior optics of the human eye [22] and raises concerns over light safety [23]. Recently, adaptive optics two-photon excitation fluorescence (TPEF) ophthalmoscopy has been demonstrated in the living macaque eye [24–26]. Many cell types throughout the retina, including ganglion cells, could be visualized, with photoreceptor outer segments providing the strongest signal [25]. Consequently, the photoreceptor layer requires the lowest light levels for two-photon imaging making it an attractive target for first application in the living human eye.

Photoreceptor cells have long been of particular interest because they contain the light-sensitive photopigment, 11-*cis*-retinal. Once this photopigment is bleached, the photoreceptors become the site where the visual (retinoid) cycle is initiated. This cycle, a chain of biochemical reactions, is fundamental to maintain visual function as it constantly regenerates the photopigment. This occurs in several steps involving numerous enzymes and chaperone proteins [27–30]. Deficiency in any of these steps due to genetic mutations, dietary factors or age will result in slowed photopigment regeneration [28], retinal disease or even blindness [28,31,32]. At an excitation wavelength of 730 nm, TPEF from photoreceptors has been shown to vary over time and to depend on the quantity of available photopigment [26]. Studies suggest that the dominant source contributing to the time-varying TPEF from photoreceptor outer segments is all-*trans*-retinol, an intermediate component of the visual cycle [33–38]. Therefore, the kinetics of all-*trans*-retinol, i.e. the production and clearance rates, are directly related to photopigment regeneration [39] and tracking the time-varying

Biomedical Optics EXPRESS

TPEF could provide diagnostic and prognostic insights into retinal diseases. In the future, this technique might serve as a clinical tool for functional assessment of the retina prior to structural defects.

An obstacle to applying *in vivo* TPEF ophthalmology in humans is ensuring the use of safe light levels. Light damage is known to be multifactorial in nature and the system comprised of photoreceptor cells and the retinal pigment epithelium (RPE) is particularly vulnerable due to the abundance of light absorbing photopigments [40]. Efficient two-photon imaging currently requires the use of sub-100 fs pulsed lasers as the pulse duration is inversely related to the likelihood that two photons arrive at the targeted fluorophore within a very short time [16]. Pulsed light sources generate peak powers that have the potential to cause mechanical, photochemical and thermal damage [40,41], however, due to the lack of data, appropriate safety standards are not well established [42]. Because of the lower efficiency of two-photon compared to conventional reflectance imaging, the retina must be exposed to higher IR light levels. Additionally, as a consequence of the nonlinear excitation, signals from chromophores with absorption spectrum in the UV range can be generated within the retina by the pulsed IR light. It is not known what impact these exposures might have on retinal structure and function. Before TPEF ophthalmoscopy can be deployed in humans, it is essential to establish light levels that are as low as possible and safe but sufficient to reliably track all-*trans*-retinol kinetics. Given the similarities between the eyes of old world monkeys and humans in terms of retinal morphology and physiology, this family of primates is the most appropriate animal model to study. Here, we examined the effects of exposure to ultrashort pulsed light in macaque to test the feasibility of safe two-photon imaging in the living human eye.

2. Methods

2.1 Animal preparation

Over the course of the study the eyes of two macaques (animal 1: macaca fascicularis, male, 8 y/o; animal 2: macaca mulatta, female, 5 y/o) were imaged. Animals were handled in accordance with a protocol approved by the University of Rochester's Committee on Animal Resources and with the ARVO policy for animal use in research. Imaging sessions with clinical devices lasted approximately 45 min. Anesthesia was induced with ketamine (6 mg/kg) and medetomidine (0.15 mg/kg). For angiographies, 7.7 mg/kg of sodium fluorescein was intraveneously administered. At the end of the imaging session, anesthesia was reversed with 0.2 mg/kg of atipamezole. High resolution retinal imaging sessions lasted for a maximum of 6 h. Anesthesia was initiated with ketamine (5-20 mg/kg), midazolam (0.25 mg/kg) and glycopyrrolate (0.017 mg/kg) and maintained with isofluorane (1.5-3%) for the duration of the experiment. The animal's body temperature was maintained at 37.8-38.9 °C with a heated air flow system and warming packs. A trained animal technician constantly monitored vital signs and recorded these every 15 min. Lactated Ringer's solution was given via intravenous drip for fluid replenishment. The paralytic rocuronium bromide (20-55 μg/kg/hour) was administered and the animal was artificially respirated. After completion of the experiment, paralysis was reversed with neostigmine (0.05 mg/kg) and glycopyrrolate (0.01 mg/kg). Pupil dilation and cycloplegia were induced with up to 4 drops of phenylephrine hydrochloride (2.5%) and tropicamide (1%). If the pupil did not fully dilate, up to 4 drops of cyclopentolate were given in addition. A lid speculum held the eye open and a contact lens lubricated with Genteal (Alcon, Fort Worth, Texas) prevented dehydration and corrected for refractive errors. A stereotaxic cart consisting of an XYZ-stage combined with a two-axis goniometer was used to align the animal's pupil with the exit pupil of the imaging system and to steer the imaging light to different retinal locations.

Biomedical Optics EXPRESS

2.2 Auxiliary imaging

In previous studies, light damage has been assessed with clinical images exhibiting at least one of the following: local intensity changes in fundus images or optical coherence tomography (OCT) images, depigmentation in color fundus photographs, window defects in fluorescein angiograms, or changes in high resolution reflectance images of photoreceptors or fluorescence images of the RPE [43–46]. Here, we employed a range of clinical and laboratory imaging techniques (see Table 1 for details).

A confocal scanning laser ophthalmoscope (cSLO; Spectralis HRA + OCT, Heidelberg Engineering, Heidelberg, Germany) was used to obtain 30° field-of-view images in each of the following modalities: blue-light reflectance (BR), blue-light autofluorescence (BAF), infrared reflectance (IR), and infrared autofluorescence (IRAF). Fourier-domain OCT scans were captured with the same instrument. A fundus camera (TRC, Topcon Corporation, Tokyo, Japan) was used to obtain 50° field-of-view fundus photographs (color and red-free) as well as fluorescein angiograms.

Additional high resolution imaging was performed with a single-photon adaptive optics scanning light ophthalmoscope (SP-AOSLO) to record lipofuscin autofluorescence of RPE. Lipofuscin fluorescence was excited with a 561 nm laser at 35 μW and imaged with an emission filter centered at 624 nm (Δ40 nm). This instrument has been described previously [45–48].

Table 1. Clinical and laboratory instruments employed to assess retinal status

Device	Modality	Wavelength [nm]		Primary contrast providing retinal structure
		excitation	emission	
cSLO (Heidelberg Spectralis)	Blue reflectance (BR)	488	488	inner retina
	Blue auto-fluorescence (BAF)	488	>510	lipofuscin within RPE [49]
	Infrared reflectance (IR)	815	815	outer retina, choroid
	Infrared auto-fluorescence (IRAF)	786	810-840	melanin within RPE and choroid [50]
OCT (Heidelberg Spectralis)		870	870	retina, choroid
Fundus photography (Topcon TRC)	Color	white[a]	white[a]	retina, pigment
	Red-free	white[a]	green[a]	retina, vasculature
	Fluorescein angiography	blue[a]	525-535	vasculature
SP-AOSLO	Visible autofluorescence	561	624/40	lipofuscin in RPE [51]
TP-AOSLO	Infrared reflectance	730 796	730/40 800/40	photoreceptors [52–54]
	TPEF	730	400-550	all-*trans*-retinol

[a]Exact spectra are not known.

2.3 Two-photon adaptive optics scanning light ophthalmoscope

A custom-built two-photon adaptive optics scanning light ophthalmoscope (TP-AOSLO) was used in this study. The instrument has been described in detail elsewhere [25,26]. The TP-AOSLO employed three light sources in the near IR: a laser diode (QFLD-850-20S, QPhotonics, Ann Arbor, MI, USA) emitting at 840 nm with maximum power output at the system's exit pupil of 50 μW for wavefront sensing, a superluminescent diode (SLD; S-790-G-I-15, Superlum, Carrigtohill, Ireland) emitting at 790 nm with maximum power output of 250 μW for confocal reflectance imaging and a pulsed Ti:Sapphire laser (MaiTai XF-1 with DeepSee attachment for dispersion compensation, Spectra-Physics, Santa Clara, CA, USA) with a tunable central wavelength between 710 nm and 920 nm for two-photon excitation and

Biomedical Optics EXPRESS

confocal reflectance imaging. The repetition rate was 80 MHz. For this study, the pulsed laser was set to a central wavelength of 730 nm (FWHM 15 nm). The second-order dispersion compensated pulse duration was ~55 fs. Adaptive optics was incorporated in the system by means of a custom Shack-Hartmann wavefront sensor (203 µm pitch, 7.8 mm focal length, 2/3x magnification between eye and sensor; Rolera XR QImaging, Surrey, Canada) and a deformable mirror (DM 97-15, ALPAO SAS, Grenoble, France). Photomultiplier tubes (H7422-40 and H7422-50, Hamamatsu Photonics, Hamamatsu, Japan) were used for detection. Non-descanned TPEF emission was collected through two filters with a transmission window from 400 to 680 nm and two filters with a transmission window from 400 to 550 nm (ET680sp-2p8 and E550sp-2p; Chroma Technology Corporation, Below Falls, VT, USA). Videos of photoreceptor structure and time-varying TPEF were simultaneously acquired in the forward and backward scan directions at a frame rate of 22.5 Hz. An average pulsed laser power of 0.5 mW at the cornea and a 1.3° x 1.1° raster scan provided sufficient signal-to-noise ratio (SNR) to reliably track TPEF and routinely image cone photoreceptors in our current TP-AOSLO.

2.4 Study design

The timeline of the safety study is laid out in Table 2. Prior to (week 0 of the study) and 48 hours after exposing the retina to the potentially hazardous pulsed laser (weeks 1, 2, and 3 of the study), the retinas of both animals were imaged with commercial clinical devices. Long-term follow-ups were made 21 weeks after the first exposure.

Table 2. Imaging and exposure time points of the safety study

Week (days) of study	cSLO & OCT	Fundus photography	Fluorescein angiography	SP-AOSLO	Exposure & TP-AOSLO
0 (0/0)	■	■	■		
1 (6/7)					■
1 (8/9)	■	■	■		
2 (13/14)					■
2 (15/16)	■	■	■		
3 (20/21)					■
3 (22/23)	■	■	■		
9/13 (62/90)				■	
22 (152/153)	■				
24 (166/167)					■

[a]Animal 1 and 2 were usually imaged in the same week but on different days. Shaded cells mark the imaging modalities that were used at indicated time points.

In weeks 1, 2 and 3 of the study, 8 near-peripheral retinal locations (1.3° x 1.1°) were exposed in each of the two monkeys to the pulsed laser with the TP-AOSLO. The procedure was as follows: The wavefront sensing light source and the 790 nm SLD for reflectance imaging were used over a field of view of 2.2° x 2° to steer to the predetermined retinal location with minimum shadows of retinal vasculature. To be able to return to the same spot for follow-ups, locations in proximity to characteristic vessel patterns were preferred. The field of view was then decreased to 1.3° x 1.1°, the SLD was disabled, the pulsed laser was enabled and focused at the photoreceptor layer. Adjusting the focus took no more than 3 s. All light sources were switched off and the retina was given 15 min to dark adapt. After this adaptation period, the retinal location was exposed for either 40 s to the minimally required power of 0.5 mW (20.4 J/cm^2) or 80 s to 1 mW (81.7 J/cm^2) of the pulsed laser light. In previous work [26], at a similar laser power of 0.75 mW, TPEF was observed to increase after dark adapation to a plateau due to stimulation of the imaging laser itself. A minimum duration of 40 s was chosen to allow the TPEF to reach the plateau. The lower exposure corresponded to 5.7 log photopic td and 3.8 log scotopic td. If photopigment regeneration is neglected for simplicity of calculation, this exposure is expected to bleach 96% of the cone photopigment and 3% of the rod photopigment [55]. The higher exposure corresponded to 6.0 log photopic td and 4.1 log scotopic td and bleached approximately 98% of the cone photopigment and

Biomedical Optics EXPRESS

10% of the rod photopigment. However, if the visual cycle is intact, less photopigment should be bleached due to regeneration.

During this exposure, reflectance videos of photoreceptor structure and TPEF videos that assessed the kinetics of the retinoid cycle were simultaneously acquired. Immediately after the exposure, an additional reflectance video was recorded using the SLD over a larger 2.2° x 2° field of view. The total exposure time of 790 nm and 840 nm light over the 2.2° x 2° was limited to 5 min. The imaging source caused an additional retinal radiant exposure of 24.9 J/cm^2 and the wavefront sensing source added 5.0 J/cm^2. During the dark adaptation period, the animal's eye drifted by no more than 0.2° with respect to the original location. Several weeks after the third exposure, single-photon excitation fluorescence from lipofuscin in the RPE cells underlying the exposed locations was measured. The retinal radiant exposure of the imaging laser in this imaging modality was <5.0 J/cm^2.

2.5 Data processing and metrics

2.5.1 Multimodal clinical imaging

To quantify any changes that could be detected with clinical imaging methods, fundus images were overlaid and manually aligned in Adobe Photoshop (Adobe Systems, Inc., San Jose, CA, USA). Exposed retinal locations were marked according to reflectance images recorded with the AOSLO. As an objective metric, the mean intensity within the central 0.5° × 0.5° region of exposed areas in fundus images acquired with the Heidelberg Spectralis was calculated and divided by the mean intensity of unexposed surrounding control areas. This value was then divided by that measured in the same locations prior to any pulsed laser exposure. A ratio less than 1 corresponded to a decrease in reflectance or autofluorescence intensity. Analogous ratios were used in previous studies to determine visible autofluorescence and IRAF changes [47,56].

2.5.2 TP-AOSLO imaging

During AO imaging, high-SNR reflectance videos and low-SNR TPEF videos were recorded simultaneously with the pulsed 730 nm laser. Dual-image registration software [57] computed eye motions from the high-SNR video and applied the correction to both the high and the low-SNR video. The same strategy of co-registration was applied for RPE imaging. Here, the high-SNR video captured photoreceptor reflectance; the low-SNR video recorded RPE autofluorescence.

Following dark adaptation, TPEF increased from the initial value at laser onset to a plateau due to stimulation of the photoreceptors with the imaging laser itself. Only TPEF within cones was extracted to increase the SNR because at 730 nm rods were hardly stimulated. Cones were identified in reflectance images and TPEF within the cone mask of the entire frame was averaged. TPEF from 50 successive frames was binned and exponential functions of the form $y = \frac{\Delta F}{F} \cdot e^{-t/\tau} + 1$ were fit to the time course. TPEF time constants τ and relative TPEF increases $\frac{\Delta F}{F}$ were extracted from the exponential fits. If the visual cycle is compromised in any way, the TPEF time course should be affected as evidenced by a change in time constants and/or relative TPEF increase.

2.6 Statistical analysis

Multifactorial (number of times the retinal location was exposed, laser power and subject) analyses of variance (ANOVAs) were used to test for significant effects of the pulsed laser exposures on fundus image brightness (reflectance and autofluorescence), TPEF time constants and relative TPEF increase. Once a statistical significance was found, one-tailed paired Student's t-tests were performed. A p-value less than 0.05 was deemed significant. No

Biomedical Optics EXPRESS

correction factors were applied. All error ranges are reported as standard errors. If no statistical significance was detected, power analyses were performed (80% power with 5% level of significance).

3. Results

3.1 Multimodal clinical imaging

Figure 1 shows fundus images of exposed retinal areas taken with the confocal SLO in each modality. Exposed retinal locations are marked in panel a. All exposures caused a significant reduction in IRAF ($p<0.001$). In contrast to other studies [47,56], the laser beam was not blanked by an acousto-optic modulator when the galvo scanner approached its return point. Therefore, areas of reduced IRAF were larger than the marked location. The change in intensity versus imaging week is shown in Fig. 2. Based on a power analysis, the smallest difference in IRAF intensity that could be reliably measured was 7%. The first exposure to 20.4 J/cm^2 decreased IRAF by 17 ± 2% with respect to baseline. The IRAF intensity was reduced with each subsequent exposure, even though the exposures were delivered a week apart (Fig. 2). After the third exposure, IRAF was reduced by 25 ± 1% compared to the baseline measurement made at the beginning of the study. Following a recovery period of 19 weeks from the last exposure, IRAF intensity had partially recovered ($p = 0.01$), but was still significantly reduced by 16 ± 3% ($p<0.001$) (Fig. 2 and Fig. 3). Exposures with 81.7 J/cm^2 had essentially the same effects but with larger magnitudes. The first exposure caused an IRAF reduction of 20 ± 2%, after the third exposure IRAF was reduced by 29 ± 2%, and 19 weeks later IRAF had recovered but was still reduced by 19 ± 1%. No significant change in intensity could be detected in the IR, BR or BAF modalities ($p = 0.66$, $p = 0.10$, $p = 0.87$). No changes were detected in color fundus images (Fig. 4(a)), fluorescein angiography (Fig. 4(b)) or OCT (Fig. 5).

A retina specialist, one of the authors, was asked to inspect all clinical modality data for possible changes potentially caused by the pulsed laser exposures. For initial analysis, exposed locations remained concealed and IRAF fundus images were withheld. In a repeated inspection, the full information was disclosed. Apart from the IRAF reduction, no other abnormalities were present.

To test whether this IRAF reduction was due to a nonlinear effect, the laser pulses were intentionally broadened by inducing dispersion, leading to a less efficient (~1/8) two-photon excitation [58]. As shown in Fig. 6, exposures with increased pulse durations led to similar reductions in IRAF intensity (low power: t-test: $p = 0.17$, minimum detectable difference: 26%; high power: t-test: $p = 0.28$, minimum detectable difference: 13%). After a single exposure to 20.4 J/cm^2, IRAF decreased by 13 ± 4%, whereas an 81.7 J/cm^2 exposure caused a decrease of 19 ± 4%.

Biomedical Optics EXPRESS

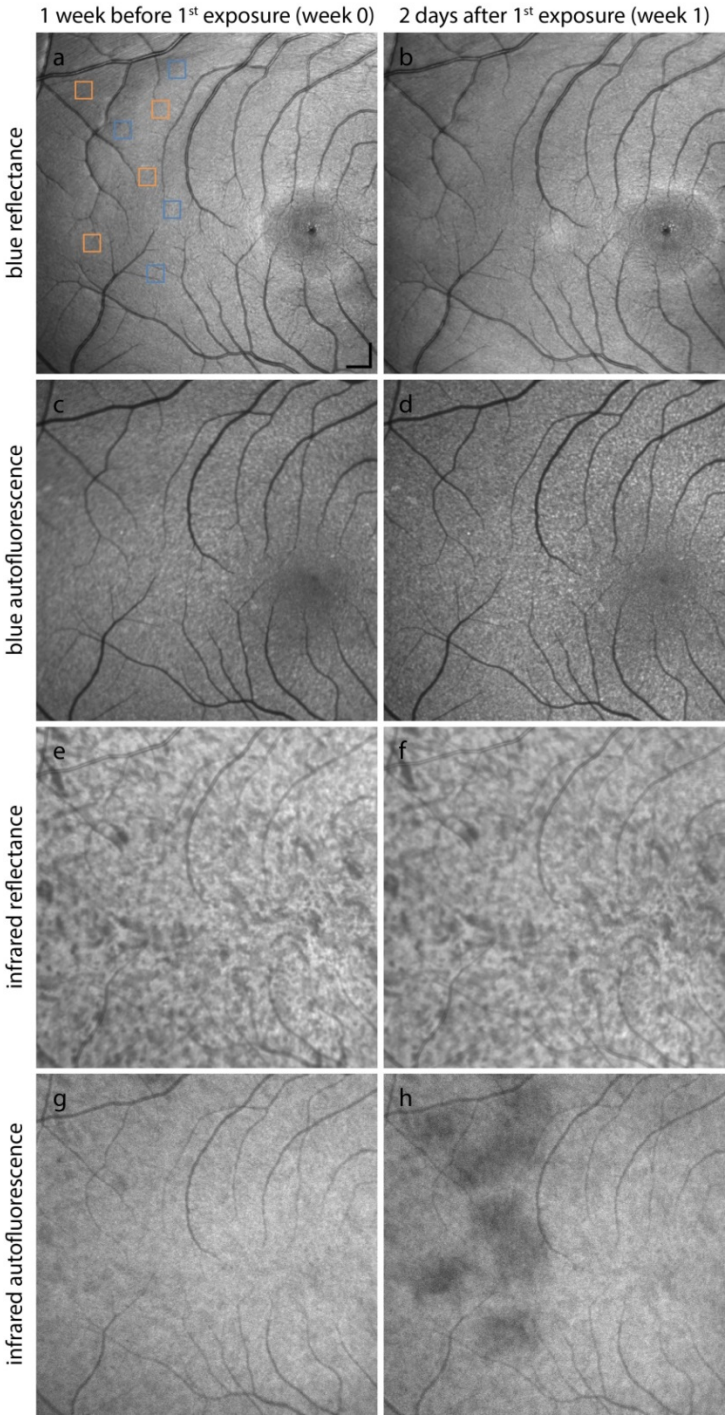

Fig. 1. Representative fundus images of animal 1 in blue reflectance (a, b), blue autofluorescence (c, d), infrared reflectance (e, f), and infrared autofluorescence (g, h) modes taken with the Spectralis before and after single exposures. Four locations received 20.4 J/cm^2 exposures with the 730-nm pulsed laser (blue boxes); four locations received 81.7 J/cm^2 (orange boxes). IRAF was reduced at the exposure sites. Scale bar: 400 µm.

Biomedical Optics EXPRESS

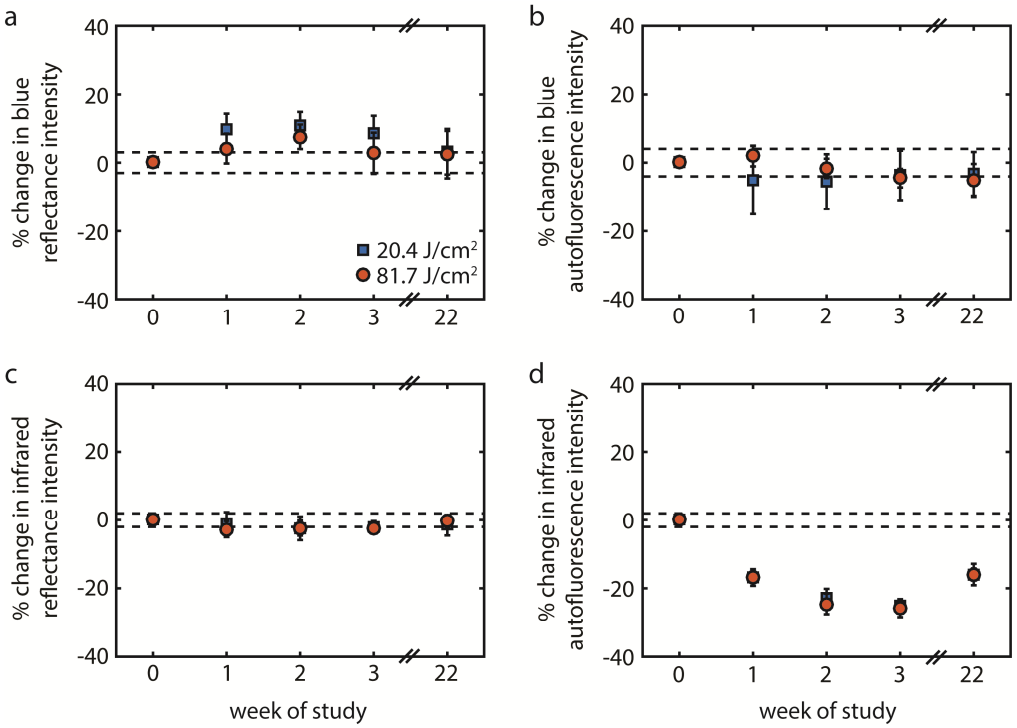

Fig. 2. Change in reflectance and autofluorescence intensity measured with the Heidelberg Spectralis following a 730-nm pulsed laser exposure. The only significant change caused by the 20.4 J/cm^2 and 81.7 J/cm^2 exposures is a significant decrease in IRAF compared to baseline ($p<0.001$). In week 22 (after a recovery period of 19 weeks), IRAF had partially recovered. Data are averaged across subjects and locations. Error bars represent standard errors and the dashed lines indicate the standard error from 8 control measurements.

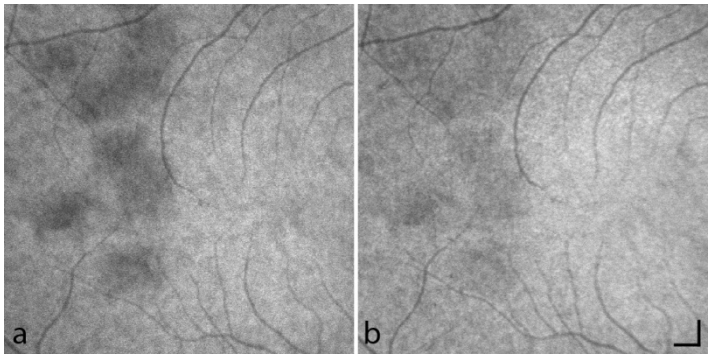

Fig. 3. IRAF fundus images of animal 1 after the 3rd exposure in week 3 (a) and in week 22 after a recovery period of 19 weeks (b). IRAF partially recovered. Refer to Fig. 1 for exposure sites. Scale bar: 400 µm.

Biomedical Optics EXPRESS

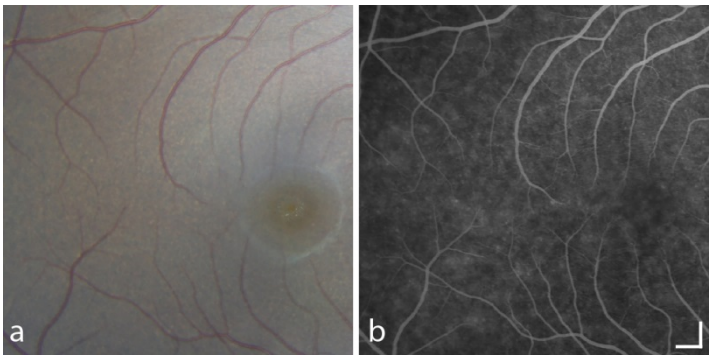

Fig. 4. Color fundus photograph (a) and fluorescein angiogram (b) of animal 1 after the third exposure in week 3. No changes were detected at the exposed locations. Refer to Fig. 1 for exposure sites. Scale bar: 400 µm.

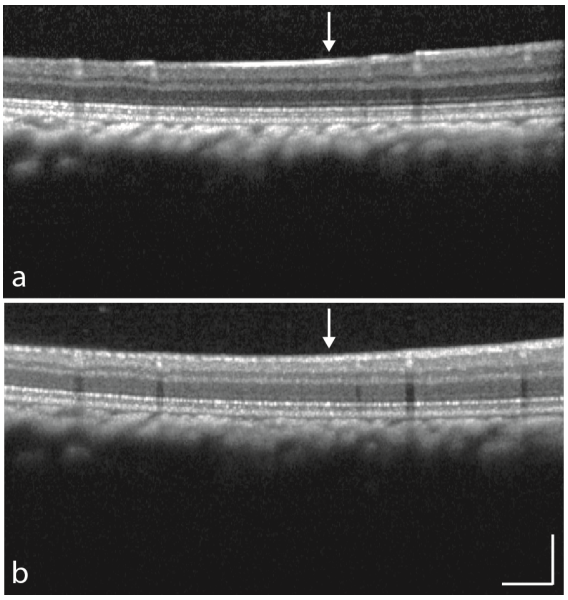

Fig. 5. Representative OCT B-scans of the same retinal location before the first exposure in week 0 (a) and after the third exposure in week 3 (b). Arrows mark the center of the 81.7 J/cm^2 exposure measuring 340 µm along the shown axis. Scale bar: 100 µm.

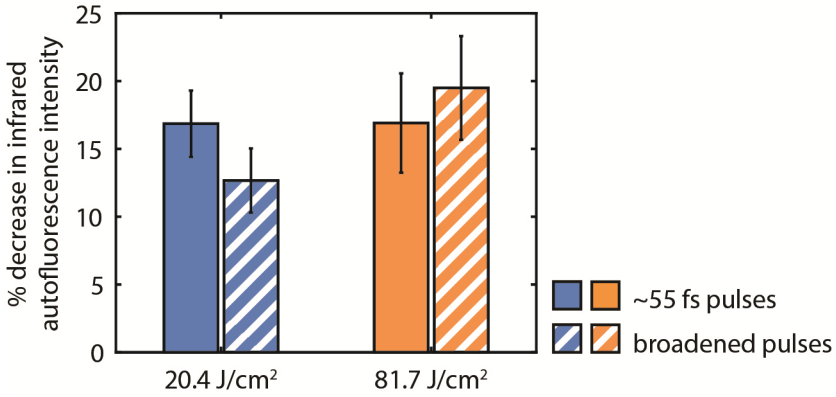

Fig. 6. Exposures with ~55 fs pulses and broadened pulses caused a similar decrease in infrared autofluorescence, implying that the decrease is unlikely to be due to a nonlinear effect.

Biomedical Optics EXPRESS

3.2 AOSLO imaging

The photoreceptor and RPE mosaic for two representative locations that were repeatedly exposed to 81.7 J/cm^2 are shown in Fig. 7. Reflectance images of the photoreceptor mosaic are shown after the first exposure in week 1 (a, d), and after three cumulative exposures in week 24 (b, d). In follow-ups, all cone photoreceptors could be re-identified and colocalized with those imaged in previous sessions. Rods could not be repeatedly resolved due to variability in image quality between imaging sessions. Nevertheless, rods appeared unchanged after repeated exposures. In RPE autofluorescence images taken 6 weeks after the third exposure, the RPE mosaic underlying the exposed retinal locations did not appear different from the surrounding areas.

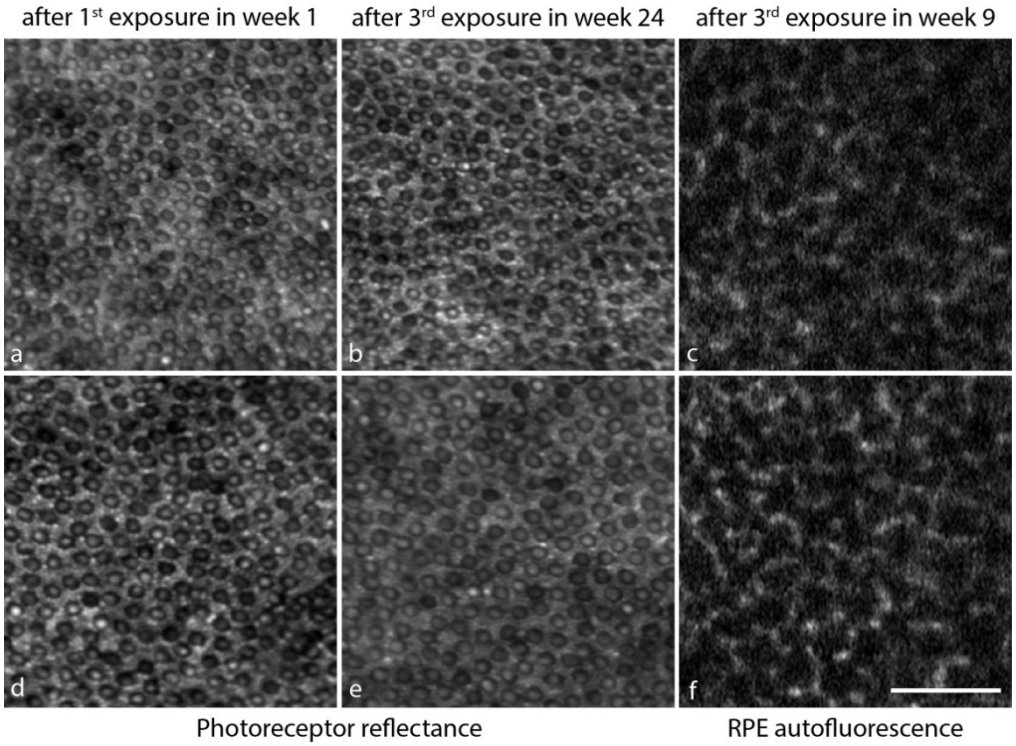

Fig. 7. Infrared reflectance images of the photoreceptor layer at two different locations (a-c and d-f) after the first exposure (a, d) and several weeks after three cumulative exposures to 81.7 J/cm^2 (b, e), and images of autofluorescence from RPE cells underlying exposed locations. Scale bar: 50 µm.

3.3 Time course of two-photon autofluorescence

Figure 8 shows the time course of TPEF for a 20.4 J/cm^2 and an 81.7 J/cm^2 exposure at two representative retinal locations. Following a dark adaptation period of 15 min, TPEF increased with the onset of the imaging laser to a plateau. Figure 9 shows the time constants and relative TPEF increase extracted from exponential fits to the TPEF time course versus imaging week for both animals. Statistical analysis revealed no significant effect of week of imaging (ANOVA: $p>0.29$), laser power ($p>0.65$), or animal ($p>0.10$) on time constants. The smallest difference in time constants that could be reliably measured was 1.8 s. The average time constant was 6.9 ± 0.4 s.

Biomedical Optics EXPRESS

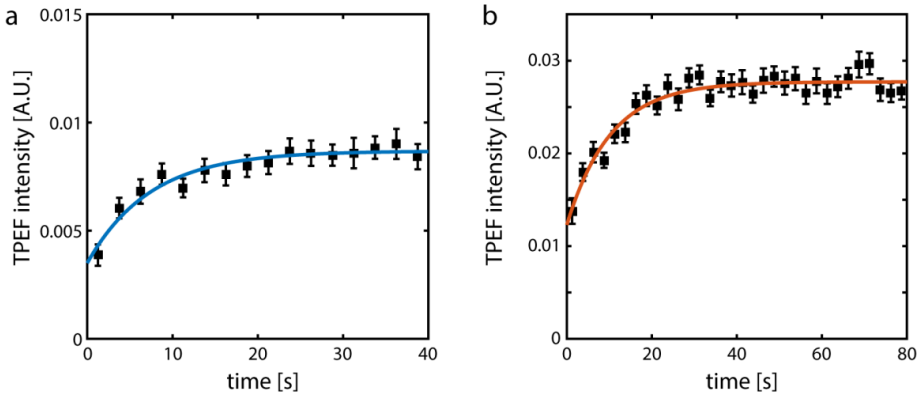

Fig. 8. TPEF time course with onset of the pulsed 730-nm laser following 15 min of dark adaptation at a sample location. For both exposures, 20.4 J/cm^2 (a) and 81.7 J/cm^2 (b), TPEF increases to a plateau. Data are well described by an exponential rise to plateau (R^2>0.91). Error bars represent standard errors.

Relative TPEF increase was 0.61 ± 0.03 when measured with the lower exposure and 0.53 ± 0.02 when measured with the higher exposure. The difference in relative TPEF increase was significant (ANOVA: p = 0.023; two-sample t-test: p = 0.014). This difference might be due to the squared increase in TPEF signal when doubling the laser power and the increased bleaching of photopigment [39]. No effect of week of imaging (p>0.26) or subject (p>0.72) on the relative signal increase was observed. The smallest difference in the relative signal increase that could be reliably measured was 0.15 and 0.04 for 20.4 J/cm^2 and 81.7 J/cm^2, respectively.

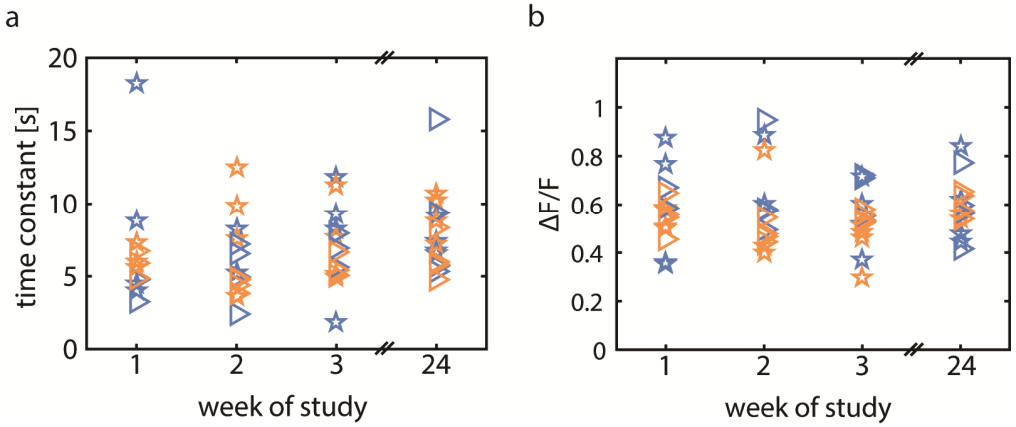

Fig. 9. Time constant (a) and relative TPEF increase ΔF/F (b) versus imaging week extracted from exponential fits to the TPEF time course for low (blue) and high (orange) exposures. Stars and triangles represent different animals.

4. Discussion

4.1 Comparison of exposures to damage thresholds and current safety standards

Retinal damage in the ultrashort laser pulse regime still lacks complete characterization. In this regime, laser peak powers are considerably higher, evoking concern for photochemical, thermal and mechanical damage [40]. Here, we compared the tested exposures to established damage thresholds and safety standards.

Special effort is required to deliver sub-100 fs pulses to the retina. The pulsed laser used in this study emitted ~55 fs pulses. Due to the chromatic dispersion properties of refractive

Biomedical Optics EXPRESS

elements in the optical setup and the eye itself [59], any pulse delivered to the retina is blurred in time [60]. The shorter the pulse duration, the broader the spectral bandwidth, and thus the stronger the blur. In this study, second-order dispersion was precompensated for pulses delivered to the retina [61]. We are not yet able to measure the pulse duration at the retina. However, based on *ex vivo* measurements on bovine eyes [60], the pulse duration can be expected to be shorter than 100 fs. In the sub-100 fs pulse regime, nonlinear optical effects such as self-focusing and plasma formation cannot be neglected [41,61]. In the ideal scenario of 55 fs, Gaussian-shaped pulses delivered to the retina with the maximum average power of 1 mW used in this study, the peak power is 214 W.

Calculations based on tested models (detailed in the Appendix) show that this peak power is 4 orders of magnitude too low to cause self-focusing. However, the ultrashort pulses could directly ionize the exposed medium and thus generate ~$6 \cdot 10^{12}$ free electrons/cm^3. Although this number is too low to cause laser induced breakdown (>10^{20} electrons/cm^3) [61] or low-density plasma (>10^{18} electrons/cm^3) [62,63], these free electrons could interact with tissue molecules and break chemical bonds in a photochemical manner.

Safety thresholds to protect against retinal damage are set forth by the American National Standards Institute and published as the ANSI Z136.1 standard [42]. However, the 2014 version of the ANSI standard does not provide exposure limits for the wavelength and pulse durations used in this study due to the lack of biological data *in vivo*. Nevertheless, the standard recommends limiting the peak irradiance to the maximum permissible exposures (MPEs) applicable to 100-fs pulses. For 100-fs pulses, the 2014 standard is at least 10 times less restrictive than the 2007 standard. MPEs were determined in a way similar to that previously published for AOSLOs employing continuous-wave light sources [43,64]. As recommended by the standard, calculations were performed for a minimal focal spot of 1.5 mrad in diameter, even though the adaptive optics in the system used here should produce a smaller and potentially more hazardous focal spot of ~0.2 mrad. Due to the low efficiency of two-photon compared to single-photon excitation [65], two-photon processes were neglected in these safety calculations. Calculations of MPEs are detailed in the Appendix. The highest exposure that was tested in this study constitutes 75% of the MPE (2014 ANSI Z136.1). Thus, we have shown that *in vivo* two-photon retinal imaging can test photoreceptor function (Fig. 8) at light levels below the ANSI MPEs.

An important requirement for *in vivo* two-photon retinal imaging is the adherence to safety limits, even in the rare case of a scanner failure. For the pulsed laser, the case of repetitive pulses of high frequency assuming a static, diffraction-limited spot at the retina was calculated as described by Delori *et al*. [46] (see Example D), to estimate the timespan for which such an exposure can be expected to be harmless. In practice, within this time frame a potential scanner failure must be detected and appropriate security measures must be taken. For the higher exposure of 81.7 J/cm^2, an exposure duration of ~0.4 s is still expected to be safe. For the lower exposure of 20.4 J/cm^2 this safety window is ~6 s which provides sufficient time to activate a mechanical shutter that blocks light going into the eye and to disable the light sources.

4.2 Effect of exposures on retinal structure and function

Previous studies of laser safety in animals showed a strong variability in terms of threshold. Therefore, we would like to point out that the inclusion of only two animals presents a limitation of this study.

As a direct measure of retinal function, the time-varying TPEF intensity after dark adaptation was quantified for the tested exposures. As reported previously, with the onset of imaging light, TPEF increased monotonically to a plateau [26]. If exposures to pulsed laser light compromise the visual cycle, the time course of TPEF after dark adaptation would be changed, resulting in altered time constants and/or relative signal increases [28,66]. No effect of exposures on TPEF time course was detected. Even though the smallest difference that

Biomedical Optics EXPRESS

could be reliably detected with this method was around 20%, it is still more localized and sensitive than standard clinical measures of retinal function, such as multifocal ERG. Moreover, the high-resolution images of the photoreceptor mosaic that are acquired simultaneously, confirmed the structural integrity of the exposure site.

The only measure that revealed a significant effect due to exposure to the imaging laser was IRAF intensity. Fundus IRAF is thought to originate mainly from the choroid and RPE with a slightly higher relative contribution of the choroid in older and darkly pigmented subjects [50]. Candidate fluorophores are oxidized melanin [67] and components closely related to melanin. IRAF reduction is most likely not due to a two-photon process since the effect was the same for exposures with longer pulse durations. A decrease in IRAF intensity as a consequence of exposure to IR light was observed in a previous study by Masella *et al*. [56], in which exposures were delivered with a continuous wave laser to human retinas. The similarity in imaging wavelength and comparable longevity of IRAF reduction with that reported by Masella *et al*. [56] suggest that we observed the same photochemical effect here. Possible explanations are therefore the bleaching of melanin or changes in fluorescence efficiency of oxidized melanin secondary to changes in the environment. Radiant exposures delivered to the retina in this study resulted in a stronger decrease in IRAF than exposures by Masella *et al*., consistent with the ~50% higher melanin absorption at 730 nm used here compared to 790 nm [50]. Masella *et al*. detected no other effect of light exposure on retinal structure or function [56] when performing Goldmann visual fields, multifocal ERG, and photopic microperimetry. Full recovery of IRAF intensity was observed 21 months after exposure. Masella et al. concluded that the effect was photochemical, however, the exact nature and cause is not yet known. Further research is needed to fully explain this phenomenon. Although the duration of the IRAF reduction effect is of concern, we could not detect a change in the visual cycle, which supports the previous functional results. We did not attempt to define an exposure threshold where IRAF is not reduced. If this effect is photochemical as Masella *et al.* concluded, it is likely that IRAF will be reduced to some extent after all exposures and any threshold would be indicative only of the minimum sensitivity to measure changes in the IRAF signal.

4.3 Future prospect of in vivo two-photon imaging of the human retina

In vivo two-photon ophthalmoscopy in humans has the potential to provide greater insight into normal visual function and retinal disease mechanisms. In the future, it could be used to track retinol creation and clearance as it occurs in the retina after bleach [26,39]. However, several differences between this feasibility study and its ultimate application to human subjects must be considered.

When measuring visual cycle kinetics in the living human eye, stabilizing the raster scan pattern on the retina is particularly important. Recent advances in real-time eye tracking can perform now with sub-cellular precision and adaptive optics imaging can be achieved routinely in patients with normal and to a certain extent compromised fixation capabilities [68,69].

The strongest two-photon signal within the retina arises from the photoreceptor layer when imaging at 730 nm. Hence, two-photon ophthalmoscopy of photoreceptors requires the least light levels and is closest to clinical translation. Ocular physiology between macaques and humans is similar but not equal. The numerical aperture is slightly smaller in humans due to greater axial lengths. Two-photon excitation efficiency depends on numerical aperture to the fourth power and, as a consequence, will probably be reduced by a factor of 1.5-2. Furthermore, visual cycle kinetics reported here are likely to be affected by the use of anesthetics. In rodents, the rate of rhodopsin regeneration can be slowed or even halted depending on the type of anesthesia [28,70]. In non-anesthetized humans, we therefore expect retinol creation and clearance to occur more quickly than has been measured in anesthetized nonhuman primates.

Biomedical Optics EXPRESS

Potential participants for initial experiments of TPEF ophthalmoscopy in the living human eye are young or middle aged adults with normal fixation and a dilated pupil diameter that is larger than the system pupil of 7.5 mm. As in the present study, measurements would be taken in the temporal periphery, at least 10° from the fovea. Exclusion criteria are any of the following: poor fixation, unclear optical media, any sign of cataract, high refractive errors or aberrations, risk to complications from topically applied dilating agents, retinal disease, photophobia and adverse psychological reactions to flashes of light.

A necessary alteration of the imaging paradigm used in this study is the addition of a visual stimulus that optimally bleaches the targeted photoreceptors. In monkey, this strategy has been successfully employed to determine retinol kinetics from rods after bleach [39]. With further improvement in TPEF detection, necessary exposures could be further reduced which will reduce stimulation of cone photoreceptors by the imaging laser and leave more room for TPEF evoked by brief visual stimuli. Two-photon ophthalmoscopy therefore promises the ability to biochemically characterize the performance of the visual cycle in different photoreceptor classes. Eventually, the efficiency of two-photon ophthalmoscopy may reach a level where imaging of retinal layers other than the photoreceptor mosaic becomes feasible. Apart from retinol, other important fluorophores like NAD(P)H, FAD, collagen, elastin and lipofuscin are excitable in the UV range. Many of these fluorophores are abundant in all living cells and can provide contrast throughout the retina [21,25]. In this way, structures that appear translucent when imaged with confocal reflectance ophthalmoscopy, such as cell nuclei in the outer and inner nuclear layer, could be visualized. Focusing in the inner retina could allow estimates of ganglion cell numbers and possibly the assessment of ganglion cell health in the living human eye. *In vivo* two-photon retinal imaging is therefore likely to become of tremendous clinical value in revealing retinal status.

Appendix

1. Threshold calculations for mechanical damage

Ultrashort pulsed lasers emit peak powers that have the potential to cause mechanical damage. On the one hand, the nonlinear dependence of the refractive index on irradiance can cause self-focusing of the laser beam. In the extreme case, the beam diameter is decreased below the diffraction limit. On the other hand, high peak powers can cause ionization and thus plasma formation. Plasma has absorptive properties that are different from those of ordinary gases. Here, the critical power for self-focusing and plasma formation was calculated and compared to the estimated peak power when exposing the retina to an average power $P_{avg} = 1\,mW$ at a wavelength $\lambda = 730\,nm$.

a) Laser peak power

Assuming Gaussian pulse shapes, the peak power of the ultrafast laser used in this study is

$$P_{peak} = 0.94 \cdot \frac{P_{avg}}{f_{rep} \cdot \tau} \approx 214\,W \tag{1}$$

with the pulse repetition frequency $f_{rep} = 80\,MHz$ and the pulse duration $\tau = 55\,fs$.

b) Self-focusing

Self-focusing occurs if the laser peak power approaches the critical power [71,72]

$$P_{cr,SF} = \frac{0.148 \cdot \lambda^2}{n \cdot n_2} \approx 1.34\,MW \tag{2}$$

Biomedical Optics EXPRESS

where the linear and nonlinear refractive indices for vitreous humor are $n = 1.336$ and $n_2 = 1.4 \cdot 10^{-13}\ esu = 43.9 \cdot 10^{-21}\ \frac{m^2}{W}$ [73], respectively.

c) Plasma formation

The irradiance threshold for plasma formation in the femtosecond laser pulse regime in ocular media is calculated following the example of Cain et al. [61] by using the first order model of Kennedy [74,75], with special attention to Kennedy, 1995 sections IV D and V F. For the ultrashort pulse regime, this model is based on the theory of multiphoton ionization in condensed media [76]. The irradiance threshold for multiphoton breakdown as derived by Kennedy is:

$$I_{cr} = \frac{\left(\frac{\rho_{cr}}{A \cdot 0.5 \cdot \tau}\right)^{1/K}}{B} \tag{3}$$

with ρ_{cr} being the critical free electron density explained below, $K = \left\langle 1 + \frac{\Delta}{\hbar \cdot \omega} \right\rangle = 4$ the number of photons required to ionize the medium when $\Delta = 6.5\,eV$ is the ionization energy of the medium and $\omega = \frac{2 \cdot \pi \cdot c}{\lambda} = 2.58 \cdot 10^{15}\ Hz$ the optical frequency where $c = 3 \cdot 10^8\ \frac{m}{s}$ is the vacuum speed of light, λ the wavelength and the parameters

$$A = \left(\frac{2}{9 \cdot \pi}\right) \cdot \omega \cdot \left(\frac{m' \cdot \omega}{\hbar}\right)^{3/2} \cdot e^{2K} \cdot \Phi(z) \cdot \left(\frac{1}{16}\right)^{K}$$

and

$$B = \frac{q^2}{m' \cdot \Delta \cdot \omega^2 \cdot c \cdot \varepsilon_0 \cdot n_0}$$

ω, K and Δ are the same as above, $\varepsilon_0 = 8.85 \cdot 10^{-12}\ \frac{C}{Vm}$ is the permittivity of free space, $n_0 = 1.336$ the index of refraction of the medium at frequency ω, $m' = 4.55 \cdot 10^{-31}\ kg$ the exciton reduced mass, $\hbar = 6.58 \cdot 10^{-16}\ eVs$ the reduced Planck constant, $q = 1.6 \cdot 10^{-19}\ C$ the electron charge, and $\Phi(z) = e^{-z^2} \cdot \sum_{n=0}^{\infty} \frac{z^{2n+1}}{n! \cdot (2n+1)}$ represents Dawson's Integral with $z = \sqrt{2K - \frac{2\Delta}{\hbar \cdot \omega}}$.

Like Cain *et al.* [61], we used Vogel *et al.*'s [62,63] definition of low density plasma (LDP), i.e. a free electron density of $\rho_{LDP} = 10^{18}\ cm^{-3}$ at which optical absorption in the plasma becomes significant. For laser induced breakdown (LIB), a higher free electron density of $\rho_{LIB} = 10^{22}\ cm^{-3}$ must be reached. The critical irradiances for LDP formation and LIB are then:

$$I_{cr,LDP} \approx 5.47 \cdot 10^4\ \frac{W}{\mu m^2}$$

Biomedical Optics EXPRESS

and

$$I_{cr,LIB} \approx 1.73 \cdot 10^5 \frac{W}{\mu m^2}$$

Corresponding critical peak powers when taking into account the diffraction limited focal spot size of ~2.49 μm^2 are therefore:

$$P_{cr,LDP} \approx 136\,kW$$

and

$$P_{cr,LIB} \approx 431\,kW$$

These values are much higher than the maximum peak power of 214 W (corresponding to the 81.7 J/cm^2 exposure) tested in this study. Using this model to calculate the free electron density generated with the tested exposure at the focal spot by rearranging Eq. (3), every laser pulse with a peak power of 214 W generates $6 \cdot 12^{10}$ free electrons/cm^3. If damage was observed following such exposures, this would most likely be a photochemical, rather than a photomechanical effect.

2. ANSI maximum permissible exposures

Light safety calculations were determined according to previously published maximum permissible exposure (MPE) estimates for AOSLOs [43,64] and pulsed lasers [64]. All calculations were based on the most recent ANSI standard for the safe use of lasers [42]. The TP-AOSLO used in this study exclusively employed wavelengths exceeding 700 nm. As a consequence, only thermal thresholds have to be taken into account. Given the comparatively low probability of a nonlinear versus a single-photon event, two-photon processes are not considered in this section. Exposure limits calculated here together with all relevant parameters are presented in Table 3.

a) Thermal limit of a continuous beam uniformly distributed over the entire field

The MPE in Watts is given in Table 5f of the ANSI standard for wavelengths $700\,nm \le \lambda \le 1050\,nm$ and exposure durations $5 \cdot 10^{-6}\,s \le t < 3 \cdot 10^4\,s$ and can be equated as:

$$MPW_{CW,th} = 1.8 \cdot 10^{-3} \cdot C_A \cdot C_E^{\,*} \cdot A_{P,7} \cdot t^{-0.25} \qquad \text{(Eq. (4)}$$

with the following parameters:

$C_A = 10^{0.002(\lambda - 700)}$ roughly represents the absorption spectrum of melanin at the wavelength λ,

$C_E^{\,*} = \frac{\alpha_{fast} + \alpha_{slow}}{2\alpha_{\min}}$ is a scaling factor for extended, rectangular sources where α_{fast} and α_{slow} are the fast and slow scan angles subtending the sides of the scan field and $\alpha_{\min} = 1.5\,mrad$, if $\alpha_{fast}, \alpha_{slow} < \alpha_{\max} = 100\,mrad$ and $t \ge 0.25\,s$, and

$A_{p,7} = (0.35\,cm)^2 \cdot \pi \approx 0.385\,cm^2$ is the area of a 7 mm diameter pupil.

b) Thermal limit of a pulsed exposure of a line segment

A pulsed line segment (PLS) exposure more closely mimics the situation of AOSLO imaging because a light source is raster scanned across the retina. During the single pulse duration $t_{\min}$, a rectangular (slit-shaped) retinal area becomes exposed. For IR light, $t_{\min} = 5\,\mu s$. The frame rate of the TP-AOSLO was $F = 22.5\,Hz$ with a scan rate of the fast scanner of $S = 14\,kHz$.

Biomedical Optics EXPRESS

One line is scanned in $\frac{1}{S} = 71\,\mu s$, meaning that in $t_{\min}$ only a fraction of a line scan is exposed. The width of the exposed rectangle is therefore theoretically the diffraction limited spot size. However, the minimal spot size considered by the ANSI standard that must be used for the following calculations is $\alpha_{\min} = 1.5\,mrad$. The length of the exposed rectangle is determined as the distance the spot scans during $t_{\min}$, that is $\alpha_{PLS} = 2\alpha_{fast} \cdot S \cdot t_{\min}$ for a galvanometric fast scanner. This line segment is traversed by $m = \frac{2\alpha_{\min} \cdot S}{\alpha_{slow} \cdot F}$ raster lines during each frame. The factor 2 only applies if the light source remains enabled for the backward scan, as it was the case in this study (ON-ratio 100%). During the total exposure, this occurs $F \cdot t$ times. Since the total number of pulses $n = m \cdot F \cdot t$ exceeds 40, the multiple pulse exposure correction factor C_P is 0.4. In this case, the MPE is given as:

$$MPE_{P,th} = 1.8 \cdot 10^{-3} \cdot C_P \cdot C_A \cdot C_E^{*} \cdot A_{P,7} \cdot t_{\min}^{-0.25} \tag{5}$$

with C_A, C_E^{*} and $A_{P,7}$ being the same as in section 2a) of the Appendix.

Table 3. Maximum permissible average power at the pupil and other relevant parameters

λ [nm]	796	840	840	730
α_{fast} [°]	2.2	2.2	1.3	1.3
α_{fast} [mrad]	38.4	38.4	22.7	22.7
α_{slow} [°]	2	2	1.1	1.1
α_{slow} [mrad]	34.9	34.9	19.2	19.2
t [s]	300	300	80[a], 40[b]	80[a], 40[b]
C_A	1.56	1.91	1.91	1.15
C_E^{*}	24.44	24.44	13.96	13.96
$MPE_{CW,th}$ **[mW]**	**6.33**	**7.75**	**6.16[a], 7.33[b]**	**3.71[a], 4.42[b]**
$t_{\min}$ [µs]	5	5	5	5
α_S [mrad]	5.37	5.37	3.17	3.17
m	42	42	71	71
n	7800	7800	2080[a], 1040[b]	2080[a], 1040[b]
$MPE_{P,th}$ **[mW]**	222.87	272.93	155.96	93.98
P [µW]	250	50	50	1000[a], 500[b]

Values marked by [a] correspond to the 81.7 J/cm^2 exposure whereas those marked by [b] correspond to the 20.4 J/cm^2 exposure. Two columns were included for the wavefront sensing source (840 nm), because this wavelength was used over imaging fields of different dimensions. Bold numbers show the limiting maximum permissible exposure.

c) Simultaneous exposures of different sources

Section 8.2.1 of the ANSI standard frames the rule for exposures from several wavelengths. These exposures are additive on a proportional basis of spectral effectiveness. Exposure safety is achieved when the sum of ratios of exposure power to MPE $\sum_i \frac{P_i}{MPE_i} < 1$. The

Biomedical Optics EXPRESS

correction factor $C_M = \left(\frac{15}{17}\right)^2$, translates the ANSI standard developed for the human eye to the smaller macaque eye, assuming that macaque and human retina are equally sensitive to damage. Since the peak irradiance is limited to the peak irradiance of a 100 fs pulse, we implemented another correction factor $C_\tau = \frac{55}{100}$ that scales the MPEs by the ratio of actual pulse duration to 100 fs. For the 20.4 J/cm^2 exposure, the minimum required exposure for two-photon imaging, the corrected sum of the ratios yields

$$\frac{1}{C_M \cdot C_\tau} \cdot \left(\frac{2.5 \cdot 10^{-4}\ W}{6.33 \cdot 10^{-4}\ W} + \frac{5 \cdot 10^{-5}\ W}{7.75 \cdot 10^{-3}\ W} + \frac{5 \cdot 10^{-5}\ W}{7.33 \cdot 10^{-3}\ W} + \frac{5 \cdot 10^{-4}\ W}{4.42 \cdot 10^{-3}\ W} \right) \approx 0.39$$

meaning that we were operating at 39% of the MPE. With the 4x greater exposure of 81.7 J/cm^2, we were operating at 75% of the MPE, since the corrected sum of the ratios is

$$\frac{1}{C_M \cdot C_\tau} \cdot \left(\frac{2.5 \cdot 10^{-4}\ W}{6.33 \cdot 10^{-4}\ W} + \frac{5 \cdot 10^{-5}\ W}{7.75 \cdot 10^{-3}\ W} + \frac{5 \cdot 10^{-5}\ W}{6.16 \cdot 10^{-3}\ W} + \frac{1 \cdot 10^{-3}\ W}{3.71 \cdot 10^{-3}\ W} \right) \approx 0.75$$

Calculating the MPEs for a variable exposure duration t between 15 and $3 \cdot 10^4$ s, the generalized formula for the maximum permitted average power of the pulsed laser can be derived:

$$E_{730} = C_M \cdot C_\tau \cdot \left(1 - \frac{2.5 \cdot 10^{-4}}{6.33 \cdot 10^{-3}} + \frac{5 \cdot 10^{-5}}{7.75 \cdot 10^{-3}} - \frac{5 \cdot 10^{-5} \cdot t^{1/4}}{1.84 \cdot 10^{-2}} \right) \cdot \frac{1.11 \cdot 10^{-2}}{t^{1/4}} \qquad (6)$$

Figure 10 shows the maximum permissible average power at the pupil according to the calculations detailed here and the exposures tested in this study.

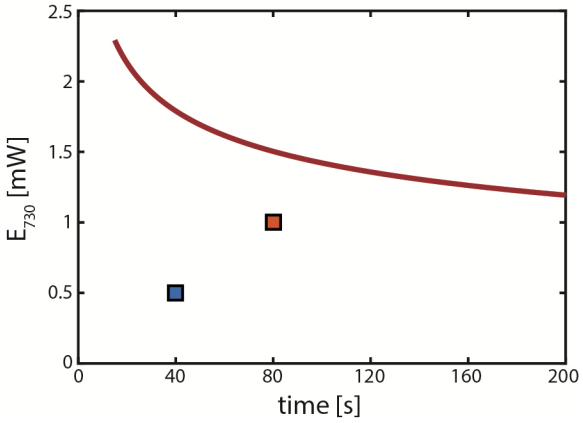

Fig. 10. The red curve shows the maximum average power of the pulsed laser that is permitted versus exposure time when keeping the same parameters for imaging as used in the described experiment. The blue (20.4 J/cm^2) and orange (81.7 J/cm^2) squares mark the exposures that were tested in this study.

d) Simulating the case of a scanner failure

Simulations of a static ultrashort pulse laser beam focused on the retina in a diffraction limited spot are presented here, to estimate the time window for security measures to become activated after a possible scanner failure. The thermal limit of repetitive pulses of very high frequency was calculated following Delori *et al*. [64] (see Example D).

Biomedical Optics EXPRESS

The single pulse MPE for a pulsed laser with a duty cycle of $\delta = f_{rep} \cdot \tau$ with $f_{rep} = 80\,MHz$ and $\tau = 55\,fs$ is:

$$MPE_{av,1} = \delta \cdot 10^{-7} \cdot \frac{A_{P,7}}{\tau} \tag{7}$$

with $A_{P,7}$ being the same as defined in section 2a.

Assuming that the reaction time for safety features to be activated is on the order of seconds, the thermal average power limit of a continuous exposure for a duration t between $5 \cdot 10^{-6}$ and 10 s is:

$$MPE_{av,2} = 1.8 \cdot 10^{-3} \cdot C_A \cdot \frac{A_{P,7}}{t^{1/4}} \tag{8}$$

For ultrashort laser pulses, the thermal average power is always the limiting MPE. By rearranging Eq. (8), the maximum duration $t_{\max}$ for which the average power at the pupil is safe can be determined:

$$t_{\max} = \left(\frac{1.8 \cdot 10^{-3} \cdot C_A \cdot A_{P,7}}{P} \right)^4$$

For the 81.7 J/cm^2 exposure, this safety window would be 0.4 s, whereas the 20.4 J/cm^2 exposure allows a reaction time of about 6 s.

Funding

This research was supported by NIH grants R44 AG043645, R01 EY022371, R01 EY021786, R01 EY004367, U01 EY025451 and P30 EY001319. The content is solely the responsibility of the authors and does not necessarily represent the official views of the National Institutes of Health. Additional support was provided by an unrestricted grant to the University of Rochester, Department of Ophthalmology from Research to Prevent Blindness, New York, NY and by the Arnold and Mabel Beckman Foundation.

Acknowledgments

The authors wish to thank Jie Zhang for his assistance in imaging the RPE and Lee Anne Schery, Amber Walker, Jennifer Strazzeri, Tracy Bubel, and Louis DiVincenti for handling the animals. AOSLO software was developed by Qiang Yang for image acquisition, by Alfredo Dubra and Kamran Ahmad for adaptive optics control, and Alfredo Dubra and Zachary Harvey for image registration. Software to mark cones in reflectance images was based on Ethan Rossi's and Kaccie Li's work at the University of California, Berkeley. The stereotaxic cart was designed by the US Air Force and constructed with modifications by Martin Gira and Mark Dietz at the University of Rochester. The authors also thank Sarah Walters, Brandi Hardy, Keith Parkins, and Kenny Cheong for their contributions.